# Investigating orbital angular momentum modes in multimode interference waveguides and revealing their mode conversion property

Afsoun Soltani  ( ✉ afsun.soltani@ec.iut.ac.ir )

Isfahan University of Technology

S. Faezeh Mousavi

University of Trieste

Zaker Hossein Firouzeh

Isfahan University of Technology

Abolghasem Zeidaabadi Nezhad

Isfahan University of Technology

Rahman Nouroozi

Institute for Advanced Studies in Basic Sciences

Article

Keywords:

# Investigating orbital angular momentum modes in multimode interference waveguides and revealing their mode conversion property

**Afsoun Soltani**[1,*]**, S. Faezeh Mousavi**[2]**, Zaker Hossein Firouzeh**[3]**, Abolghasem Zeidaabadi Nezhad**[4]**, and Rahman Nouroozi**[5]

[1,3,4]Department of Electrical and Computer Engineering, Isfahan University of Technology, Isfahan 8415683111, Iran
[2]Department of Physics, University of Trieste, Trieste 34127, Italy, and CNR-INO, National Institute of Optics, Trieste 34149, Italy
[5]Department of Physics, Institute for Advanced Studies in Basic Sciences, Zanjan 45195-1159, Iran
[*]afsun.soltani@ec.iut.ac.ir

## ABSTRACT

Orbital angular momentum (OAM) modes of light have aroused a widespread interest in quantum and classical communications. Their various integrated photonics applications require devices and circuits for miniaturization, improved performance, and advanced performance. Accordingly, in this work, the propagation of OAM modes in multimode interference (MMI) waveguides as the basic elements in many integrated optical devices is studied to utilize their benefits in integrated OAM applications. OAM modes shape the field-splitting and OAM-maintaining images at the specific lengths of an MMI waveguide. As the most effective parameters on the properties of these generated images, width of the MMI waveguide, topological charge ($l$) and waist radius of the OAM modes are investigated. Power overlap integral (POI) and mode purity are used to evaluate the quality of images. The investigations show that the images produced in wider waveguides are purer (up to $92.43\%$). Furthermore, for the higher order of OAM modes ($|l| > 1$), the higher values of POI could be achievable by enlarging the width of the waveguides (up to $93.93\%$ for $l = \pm 6$ and $81.6\%$ for $l = \pm 7$). It is also demonstrated that mode conversion between even order of OAM modes with opposite topological charges can occur at OAM-maintaining length of the MMI waveguides which is the most outstanding achievement of this survey for optical communication systems.

## Introduction

Pioneered by Allen in 1992[1], light beams with the phase dependence of $exp(il\phi)$ carry OAM, independent of the polarization state, where $\phi$ is the azimuthal angle, and $l$ indicates the topological charge ($l = \pm 1, \pm 2, ....$). Topological charge represents the number of twists the light does in one wavelength. OAM modes with different topological charge values, are theoretically unbounded and orthogonal to each other. They introduce a new degree of freedom and can therefore be effectively exploited to enhance the capacity of an optical communication link[2].

Conventional techniques for generation and manipulation of OAM modes involve the bulk devices such as spatial light modulators[3–5], spiral phase plates[6], q-plates[7,8], and fiber gratings[9,10]. Due to the complexity of optical alignment[9] and the necessity of precise control of parameters[11] it is difficult for these bulk devices to build low-loss systems. Moreover, they usually suffer from slow switching rates and limited the number of guided OAM modes[12]. Compared to the bulk optics, integrated implementations have been attracted due to the significant advantages in reliability, miniaturization and scalability[13]. Several integrated photonic circuits using devices such as microrings[13–16] and circular grating couplers[17,18] were reported as integrated solutions for OAM mode generation and manipulation. These devices rely on complicated phase-sensitive arrayed waveguide structures with a large number of electrical contacts for phase calibration. Furthermore, a passive hybrid 3D photonic integrated circuit was demonstrated as an OAM multiplexer and demultiplexer[19], where the tuning of OAM requires an additional spatial switching stage between the OAM demux output waveguides. However, these integrated circuits were convoluted for reconfiguration and their application was limited to a few modes. Hence, they do not offer a satisfying solution for optical interconnection systems[20].

Moreover, the implementation of rectangular waveguides for generation and manipulation of OAM modes, has been recently explored to exploit the outstanding features of these modes in more complex integrated devices. An on-chip integrated structure including silicon waveguides and couplers has been proposed, which can produce OAM modes with $l = \pm 1$[21]. A rectangular waveguide with a single trench has been also designed to generate OAM modes with $l = \pm 1$[22]. In addition, the integrated

rectangular platforms have been represented to generate OAM beam only on the longitudinal component of the electric field which made the application of proposed platforms complicated[23–25]. Furthermore, the investigation of spin and orbital angular momentum of optical fields in a silicon channel waveguide has been proposed based on the superposition of two quasi-TE modes which are limited to the first order of OAM modes[26]. In another recent work, the design approach to a grating coupler for in-plane generation and propagation of quasi-TE vortex modes with azimuthal order of $l = \pm 1$ within photonic integrated circuits has been suggested[27].

In addition to the previous approaches, a novel and actually neglected choice for OAM applications, MMI structures can be introduced which have many interesting features, such as their compact size, low sensitivity to fabrication parameters, and ease of fabrication[28]. In the last few years, MMI structures, based on the interference between the modes of a multimode waveguide, have been widely used in both one and two dimensions as the basic element in many integrated optical devices such as optical beam splitters[29–31], mode convertors[32], couplers[33], wavelength-division (de)multiplexers[34], and switches[35]. In one dimensional (1D) MMI devices the waveguide is single mode in the transverse dimension and multimode in the other dimension, whereas in two dimensional (2D) devices, MMI waveguides are multimode in both horizontal and vertical directions[36]. In order to carry the power by higher order modes with 2D field distributions, 2D MMI devices are required. From this point of view, 2D MMI structures can be utilized for OAM modes transmission. The use of 2D MMI structures for OAM modes, was first introduced by describing the self-imaging properties of OAM modes in MMI waveguides[37]. However, these structures still have many unknown potentials in using OAM modes which can make them an attractive and practical part of many integrated circuits such as power splitters, couplers, convertors and switches. In addition to the application of such devices in communication systems, optical imaging and manipulation are the other fields that MMI structures can be utilized in.

Accordingly, in this work, the propagation of OAM modes in square cross-sectional 2D MMI waveguides is studied. OAM modes form the field-splitting and OAM-maintaining images at the specific lengths of an MMI waveguide[37]. The properties of these images are investigated by considering three main parameters including the width of the waveguide, the waist radius of the OAM mode and its topological charge. It is also represented theoretically, and confirmed by simulation results that OAM modes with odd and even values of $l$ have different behaviour in MMI waveguides. For odd order of OAM modes, the generated images at the OAM-maintaining length of an MMI waveguide have the same topological charge as the input mode. Whereas for the even order modes, the topological charge of the produced image is reversed at this length. In other words, the propagation of an OAM mode with $l$ through an MMI waveguide leads to shape an OAM mode with $-l$ at its OAM-maintaining length. In addition to $l$, the propagation of OAM modes in MMI waveguides are affected by the width of MMI waveguide and the WR of input mode. These parameters are chosen in the ranges of 15 $\mu m$ to 60 $\mu m$, and 1.5 $\mu m$ to 3.5 $\mu m$, respectively for the investigation purposes of this paper. The properties and quality of the images along waveguides influenced by the referred parameters are discussed for OAM modes with odd and even values of $l$, separately.

The rest of the paper is organized as follows. In "Theory" the theory of beam propagation in MMI waveguides is outlined. "Results and discussion" gives simulation results and discussion, and finally, "conclusion" is devoted to the concluding remarks.

## Theory

As mentioned in 'Introduction' section, 2D MMI waveguides support multiple modes in both horizontal and vertical directions. The analysis of these structures can be performed by extending the guided mode propagation analysis method of 1D MMI structures to the 2D case.

The guided modes of a 2D MMI waveguide with $W_x$ lateral width and $W_y$ vertical width in $X$ and $Y$ directions, respectively, have the form of following equation[38]:

$$\psi_{uv}(x,y) = \psi_u(x)\psi_v(y) = sin(\frac{\pi(u+1)x}{W_x})sin(\frac{\pi(v+1)y}{W_y}),$$
(1)

where $u, v = 1, 2, 3, ...$ are the mode orders in $X$ and $Y$ directions, respectively. The corresponding longitudinal propagation constants satisfy as:

$$\beta_{uv}^2 = k^2 n_g^2 - \left(\frac{\pi(u+1)}{W_x}\right)^2 - \left(\frac{\pi(v+1)}{W_y}\right)^2,$$
(2)

where $k$ indicates the wave number, $k = \frac{2\pi}{\lambda_0}$. $\lambda_0$ is the working wavelength in vacuum and $n_g$ represents the refractive index of the multimode waveguide. Neglecting the reflected field as well as the power coupled to the radiative modes, the incident field of $\Psi(x, y, 0)$ can be expressed as a superposition of the infinite numbers of guided modes as:

$$\Psi(x,y,0) = \sum_{u=0}^{\infty}\sum_{v=0}^{\infty}C_{uv}\psi_{uv}(x,y),$$
(3)

where,

$$C_{uv} = \frac{4}{W_x W_y} \int_0^{W_x} \int_0^{W_y} \Psi(x,y,0)\psi_{uv}(x,y)dxdy. \tag{4}$$

After propagating a distance $L$ in the waveguide, the field profile $\Psi(x,y,L)$ can be expressed as:

$$\Psi(x,y,L) = \sum_{u=0}^{\infty} \sum_{v=0}^{\infty} \Psi(x,y,0)e^{j(\omega t - \beta_{uv}L)}. \tag{5}$$

Taking the foundational mode out of the summation and using the paraxial approximation for the propagation constant in equation (2), the field profile can be written as:

$$\Psi(x,y,L) = e^{j(\omega t - \beta_{00}L)} \times \sum_{u=0}^{\infty} \sum_{v=0}^{\infty} \Psi(x,y,0)e^{j\frac{u(u+2)\pi L}{3L_{\pi x}}} e^{j\frac{v(v+2)\pi L}{3L_{\pi y}}}, \tag{6}$$

which $L_{\pi x}$ and $L_{\pi y}$ are the coupling lengths between the two lowest order modes in $X$ and $Y$ directions, respectively, as:

$$L_{\pi x} = \frac{\pi}{\beta_{00} - \beta_{10}} = \frac{4n_g W_{xeff}^2}{3\lambda_0}, \tag{7}$$

and

$$L_{\pi y} = \frac{\pi}{\beta_{00} - \beta_{01}} = \frac{4n_g W_{yeff}^2}{3\lambda_0}. \tag{8}$$

In these equations $W_{xeff}$ and $W_{yeff}$ denote the effective waveguide thicknesses. The former in $X$ and the later in $Y$ directions, as:

$$W_{xeff} = W_x + \frac{\lambda_0}{\pi\sqrt{n_g^2 - n_c^2}}, \tag{9}$$

and

$$W_{yeff} = W_y + \frac{\lambda_0}{\pi\sqrt{n_g^2 - n_c^2}}, \tag{10}$$

with $n_c$ the cladding refractive index[39].

In multimode waveguides, an input field profile can be reproduced in single or multiple images at the periodic intervals along the propagation distance of the waveguide. This property is called self-imaging[28]. In equation (6), the distance $L$ to produce self-imaging can be expressed as:

$$L = (\frac{S_x}{N})3L_{\pi x} = (\frac{S_y}{M})3L_{\pi y}, \tag{11}$$

where $N$ and $M$ are the positive integers without common divisors with the positive integers $S_x$ and $S_y$, which are the positional numbers in $X$ and $Y$ directions, respectively. For simplicity, in the following discussion, $S_x = S_y = 1$, which is also a common practice for the shortest device length.

For a central input field in a 2D square cross-sectional MMI waveguide with $W_x = W_y = W$, if $N = 2K$, where $K$ is an integer, the number of images at the length $L = 3L_c/N$ can be decreased. If $K$ is an odd number, the number of reproduced self-images is $K$ for both symmetric and antisymmetric inputs. For an even integer $K$, if the input field is symmetric, self-images appear at the output, while for the anti-symmetric input fields, field-splitting imaging occurs at the output[37]. OAM modes always have the anti-symmetric field components. With the consideration of obtaining the shortest device length, OAM-maintaining and field-splitting occur for $K = 1$ and $K = 2$ at the lengths of $3L_c/2$ and $3L_c/4$ of the 2D square cross-sectional MMI waveguide, respectively.

## Results and discussion

In order to figure out the self-imaging phenomena for OAM modes in MMI waveguides, the mode propagation inside these waveguides is simulated using beam propagation method (BPM) by the commercially available simulation software package OptiBPM 13. All the simulations assume a silicon waveguide ($n_g = 3.45$) surrounded by silica ($n_c = 1.45$) at the working wavelength of $\lambda_0 = 1550\ nm$. The detailed consideration of this phenomena is performed by studying three main parameters. The first one that is related to the physical structure of the MMI waveguide, is the waveguide's width. This parameter directly specify the waveguide's lengths to generate the field-splitting and OAM-maintaining images. The studied widths are in a range of 15 $\mu m$ to 60 $\mu m$. Figure 1 indicates the calculated OAM-maintaining lengths for these scanned waveguides. The half of these lengths are the field-splitting lengths of the waveguides. This figure shows that the wider waveguides need the longer length to produce the self-image.
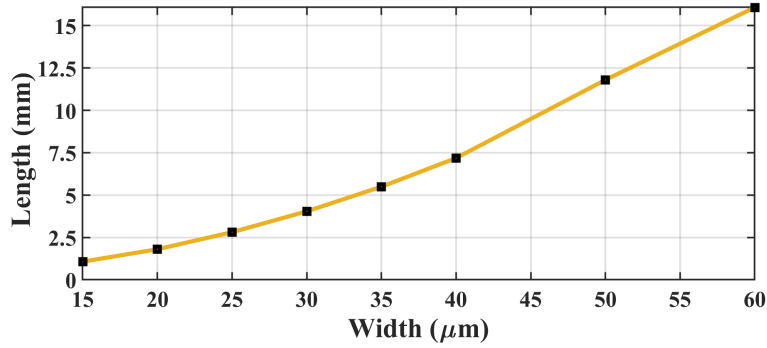


**Figure 1.** OAM-maintaning lengths for the waveguides' widths in a range of 15 $\mu m$ to 60 $\mu m$. The wider waveguides need the longer length to produce the self-image.

Two other parameters which are related to the properties of OAM modes, are WR and the order of the topological charge. The effect of these parameters can be evaluated by consideration of the POI between the input mode ($E_1$) and the output generated image ($E_2$), which is expressed as:

$$POI = \frac{|\int\int_S E_1(x,y)E_2^*(x,y)dxdy|^2}{\int\int_S |E_1(x,y)|^2\ dxdy\int\int_S |E_2(x,y)|^2\ dxdy}. \tag{12}$$

Investigating the effect of WR, the OAM modes with WR in a range of 1.5 $\mu m$ to 3.5 $\mu m$ are propagated along the waveguides with the specified widths in figure 1. The results are given in Table 1 for the calculated POI (%) between the input first order of OAM modes with $l = \pm 1$ and the output produced images. They imply that for each waveguide's width, the calculated POI increases with increasing WR of the input mode. In addition, the propagated modes with lower values of WR need wider waveguides to provide higher values of the POI. This deduction is true for OAM modes with any order of topological charge.

The topological charge of OAM modes as the third parameter studied in this paper is separately discussed for odd and even order modes as follows.

### OAM modes with odd values of *l*

To demonstrate the behaviour of OAM modes in MMI waveguides more precisely, the POI graphs along the waveguides are shown in figure 2 for the concentric input OAM modes of $l = \pm 1$. As discussed before, the length $3L_c/4$ is where the field-splitting occurs. This length is specified in figure 2 for the considered waveguides mentioned in figure 1. The graphs show that the input mode decomposition is started simultaneously as its propagation and is completed at $L = 3L_c/4$, where the POI is near zero. Then, the image is gradually formed and fully generated at $L = 3L_c/2$, where the POI again leads to near 1. The graphs also show that the increase in WR of the input modes leads to non-zero overlap integral at the field-splitting length ($3L_c/4$) which is well recognizable based on figure 3. This figure illustrates the normalized power distributions of split fields (top row) and its display in dB unit (bottom row) at the length $3L_c/4$ of the MMI waveguide with $W = 20\ \mu m$ for input OAM modes of $l = \pm 1$ with $WR = 1.5\ \mu m$ (a), 2 $\mu m$ (b), 2.5 $\mu m$ (c), 3 $\mu m$ (d), and 3.5 $\mu m$ (e). The top plots in this figure indicate that the spatial distribution of the split fields grows by increasing in WR. The bottom plots display that this growth leads to obtaining significant power around the center of the waveguides which causes the mentioned non-zero POI at the split lengths for the greater amount of the input WR. Thus, in order to fully utilize the benefits of field decomposition of OAM modes at

**Table 1.** The calculated POI (%) between the input OAM modes with $l = \pm 1$ and the output produced images for the waveguides' widths ($W$) specified in figure 1.

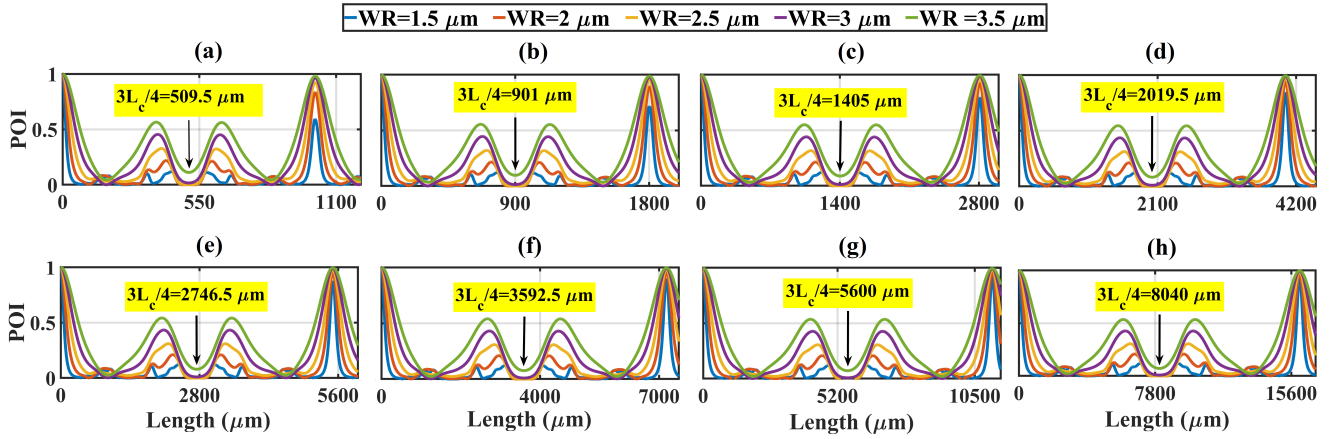| W ($\mu m$) | WR ($\mu m$) | | | | |
|---|---|---|---|---|---|
| | 1.5 | 2 | 2.5 | 3 | 3.5 |
| 15 | 59.15 | 83.65 | 92.83 | 96.47 | 98.07 |
| 20 | 71.75 | 89.65 | 95.58 | 97.84 | 98.82 |
| 25 | 79.54 | 92.84 | 96.68 | 98.53 | 99.20 |
| 30 | 84.47 | 94.71 | 97.79 | 98.92 | 99.41 |
| 35 | 87.62 | 95.80 | 98.22 | 99.12 | 99.51 |
| 40 | 89.99 | 96.68 | 98.62 | 99.33 | 99.64 |
| 50 | 92.89 | 97.67 | 99.03 | 99.53 | 99.74 |
| 60 | 94.53 | 98.22 | 99.26 | 99.64 | 99.80 |



**Figure 2.** POI graphs along the specified waveguides in figure 1 ($W = 15, 20, 25, 30, 35, 40, 50, and\ 60\ \mu m$) (a-h). The input OAM modes have the topological charges of $l = \pm 1$ with WR in a range of 1.5 $\mu m$ to 3.5 $\mu m$. The input mode decomposition is started simultaneous to its propagation, and is completed at $L = 3L_c/4$, where the POI is near zero. Then, the image is gradually formed and fully generated at $L = 3L_c/2$, where the POI again leads to near 1.

field-splitting length of MMI waveguides, it should be considered that WR of the input mode is chosen in such a way that the POI along the waveguide is zero at the filed splitting length. On the other hand, the input modes with higher values of WR have lower POI values at OAM-maintaining length. Therefore, there is a trade-off between the WR of the input mode and the POI of the generated image, which makes it challenging to choose a suitable input WR depending on the application of the structure.

For odd order of OAM modes with $|l| > 1$, the location of the split fields is same as for $l = \pm 1$ at four sides of the MMI waveguide cross section as shown in figure 4 for the MMI waveguide's width of 20 $\mu m$. This figure illustrates the normalized power distributions of split fields at the field-splitting length of the MMI waveguide for input OAM modes of $l = \pm 3$ (a), $l = \pm 5$ (b), $l = \pm 7$ (c), and $l = \pm 9$ (d). Additionally, figure 5 demonstrates the calculated POI between the input OAM modes of $l = \pm 1$ to $\pm 9$ with $WR = 2\ \mu m$ and the output generated images for different MMI waveguides' widths. The graphs imply that for the higher order of OAM modes, the higher values of POI could be achievable by enlarging the width of the waveguides.

***OAM modes with even values of*** $l$

For OAM modes with even values of $l$, the OAM-maintaining length $3L_c/2$ is where the generated image has reversed charge in comparison with the input mode. While for odd values of $l$, the produced image at this length has the same charge as the input mode. Mathematics behind this fact can be explained as the following.

Generally, any order of OAM mode field can be indicated as the superposition of odd and even mode fields as[40]:

$$f_{OAM}(x,y) = f_{odd}(x,y) \pm i f_{even}(x,y), \tag{13}$$

where the $\pm$ sign is determined by the sign of OAM order. The odd and even parts of this equation can be further represented into symmetric or anti-symmetric field functions ($f_S$ or $f_A$) in $X$ or $Y$ directions. These representations for odd and even order
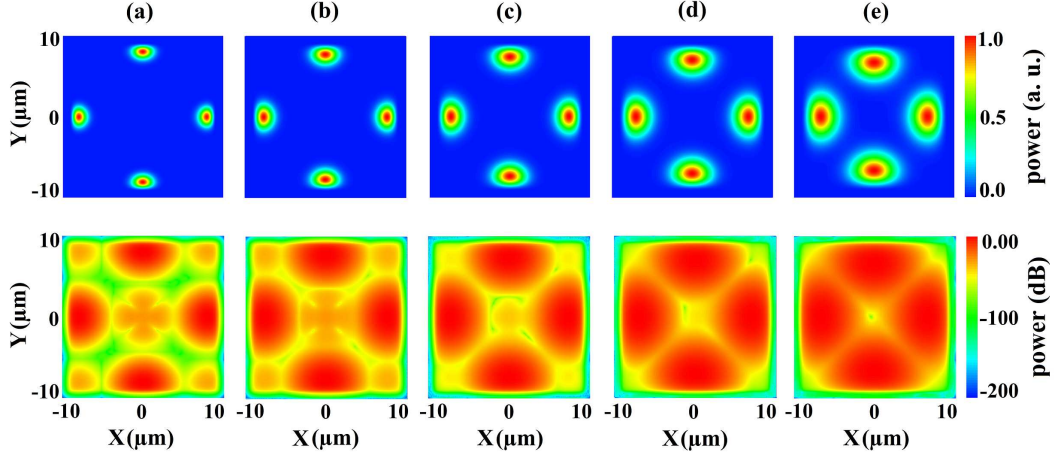
**Figure 3.** Normalized power distributions of the split fields (top row) and its display in dB unit (bottom row), at length $3L_c/4$ of an MMI waveguide with $W = 20\ \mu m$ for input OAM modes of $l = \pm 1$ with $WR = 1.5\ \mu m$ (a), $2\ \mu m$ (b), $2.5\ \mu m$ (c), $3\ \mu m$ (d), and $3.5\ \mu m$ (e). The top plots indicate that the spatial distribution of the split fields grows by increasing in WR. The bottom plots display that this growth leads to obtaining significant power around the center of the waveguides which causes non-zero POI at the split lengths for the higher values of WR.
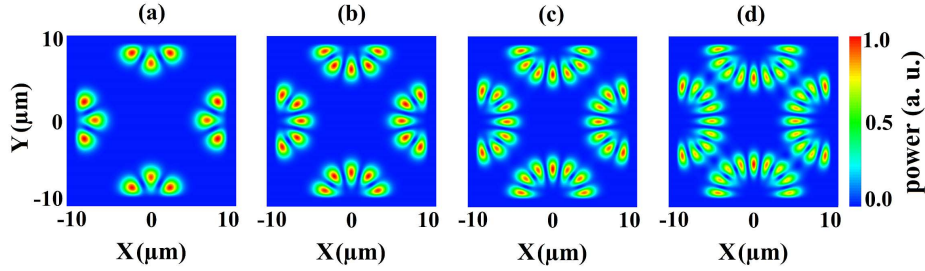


**Figure 4.** Normalized power distributions of the split fields at the field-splitting length of an MMI waveguide with $W = 20$ $\mu m$ for the input OAM modes of $l = \pm 3$ (a), $l = \pm 5$ (b), $l = \pm 7$ (c), and $l = \pm 9$ (d).

OAM modes are respectively, as[37]:

$$f_1(x,y) = f_S(x)f_A(y) \pm if_A(x)f_S(y), \tag{14}$$

and

$$f_2(x,y) = f_A(x)f_A(y) \pm if_S(x)f_S(y). \tag{15}$$

With substitution of these functions in equation 6 and consideration of obtaining one image at the center of an square cross sectional 2D MMI waveguide, the output field profiles at length $3L_c/2K$, $K = 1$ can be written as:

$$\Psi_1(x,y,L) = f_S(x)f_A(y)e^{j(\theta_S(x)+\theta_A(y))} \pm if_A(x)f_S(y)e^{j(\theta_A(x)+\theta_S(y))}, \tag{16}$$

and

$$\Psi_2(x,y,L) = f_A(x)f_A(y)e^{j(\theta_A(x)+\theta_A(y))} \pm if_S(x)f_S(y)e^{j(\theta_S(x)+\theta_S(y))}, \tag{17}$$

where $\theta_S$ and $\theta_A$ are the symmetric and anti-symmetric phase terms, respectively, as:

$$\theta_S(x) = \theta_S(y) = (\frac{K^2}{2K} + \frac{1}{4})\pi = \frac{3}{4}\pi, \tag{18}$$
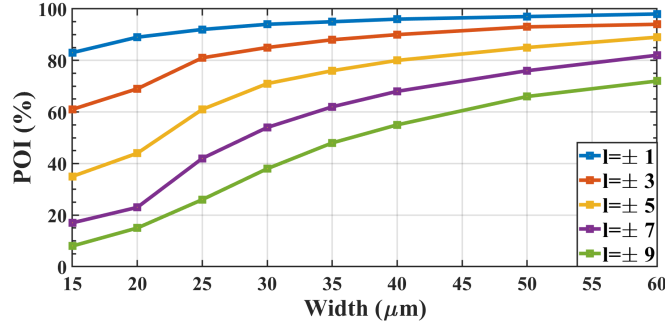
**Figure 5.** The calculated POI between the input OAM modes of $l = \pm 1$ to $\pm 9$ with the waist radius of $2\ \mu m$ and the corresponding output generated images.
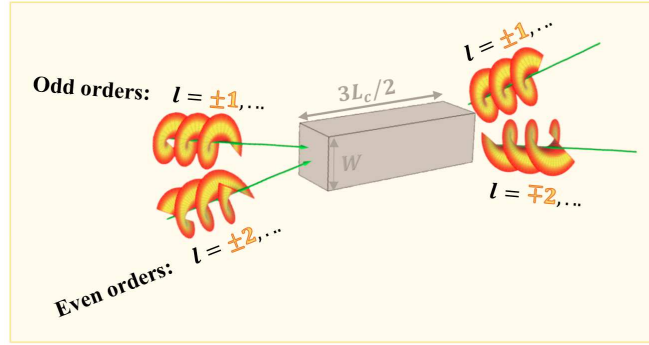


**Figure 6.** Schematic diagram of an square cross-sectional 2D MMI waveguide with the length $L = 3L_c/2$. The waveguide acts as a charge converter for OAM modes with even values of $l$.

and

$$\theta_A(x) = \theta_A(y) = (\frac{K^2}{2K} - \frac{1}{4})\pi = \frac{\pi}{4}. \tag{19}$$

Hence:

$$\Psi_1(x,y,L) = e^{(j\pi)}(f_S(x)f_A(y) \pm if_A(x)f_S(y)), \tag{20}$$

and

$$\Psi_2(x,y,L) = e^{(j\frac{\pi}{2})}(f_A(x)f_A(y) \mp if_S(x)f_S(y)). \tag{21}$$

The comparison between equations 20 and 14 as well as 21 and 15 clearly imply that the topological charge of odd order OAM modes remains unchanged after passing through the length $3L_c/2$ of the MMI waveguide, whereas the charge of even order modes is reversed. Therefore, it can be inferred that an MMI waveguide with the length $3L_c/2$ acts as inherent charge converter for OAM modes with even values of $l$. This fact is schematically shown in figure 6.

Declaring the mentioned mode conversion property, the propagation of second, fourth and sixth order of OAM modes along a 40 $\mu m$ width MMI waveguide is shown in figure 7. In this figure, left and right columns display the normalized power distributions and phase patterns of the input (top rows) OAM modes of $l = +2$ (a), $l = +4$ (b), and $l = +6$ (c), and the output (bottom rows) generated images of $l = -2$ (a), $l = -4$ (b), and $l = -6$ (c). Comparing the phase patterns of the input modes and the generated images, that are respectively clockwise and counterclockwise for each twist, it is clear that the topological charges are reversed.

In order to find out how well a 2D MMI waveguide can work as a charge converter for even order of OAM modes, the
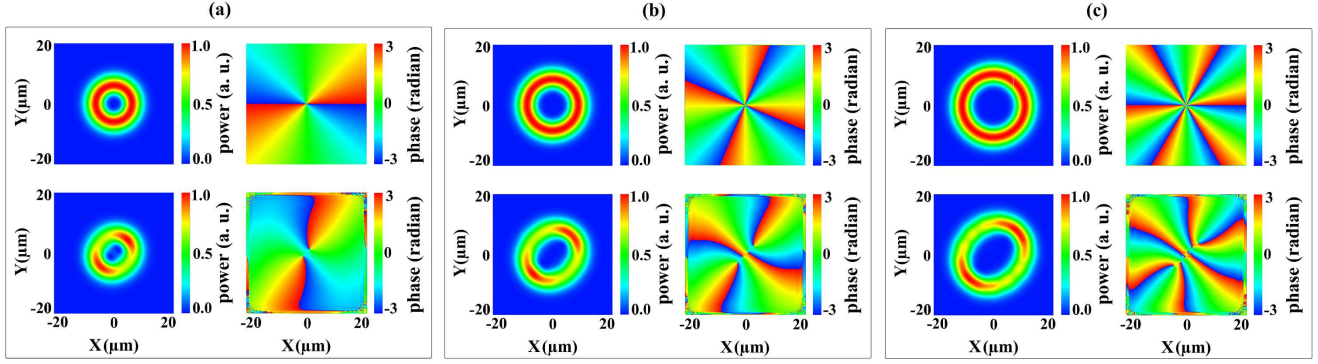
**Figure 7.** Normalized power distributions (left) and phase patterns (right) of the input (top rows) OAM modes of $l = +2$ (a), $l = +4$ (b), and $l = +6$ (c), and output (bottom rows) generated images of $l = -2$ (a), $l = -4$ (b), and $l = -6$ (c) for an MMI waveguide with 40 $\mu m$ width. A comparison between the phase pattern of the input modes and the generated images that are respectively clockwise and counterclockwise for each twist, clearly implies that the topological charges are reversed.
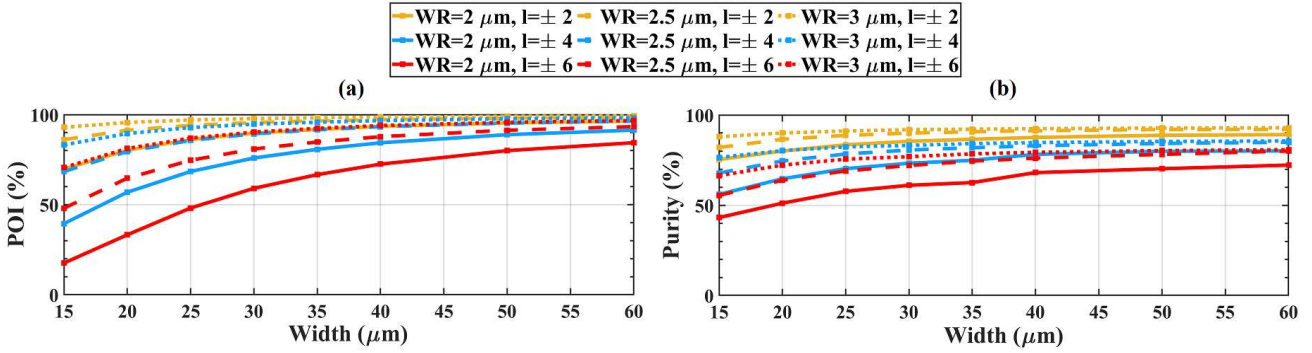


**Figure 8.** The Calculated POI (a) and purity (b); while the MMI waveguides with width in a range of 15 $\mu m$ to 60 $\mu m$ are excited by the second, fourth and sixth orders of the input OAM modes with WR in a range of 2 $\mu m$ to 3 $\mu m$. Both the calculated POI and purity are enhanced by increasing in the waveguide's width and WR of the input mode.

purity of the generated images, $E(\rho, \theta)$, are calculated using[41]:

$$purity = \frac{\int_0^\infty | \int_0^{2\pi} E(\rho, \theta) \frac{\exp(-il\theta)}{\sqrt{2\pi}} d\theta |^2 \rho d\rho}{\int_0^\infty \int_0^{2\pi} | E(\rho, \theta) |^2 d\theta \rho d\rho}. \tag{22}$$

Furthermore, the POI between output generated image and the desired corresponding OAM mode are studied. Calculated POI and purity for the mentioned waveguide in figure 7 with $W = 40\ \mu m$ and the propagated OAM modes with $WR = 3\ \mu m$ are reported in table 2.

Figure 8, indicates the calculated POI and purity, when the second, forth and sixth orders of input OAM modes with WR in a range of 2 $\mu m$ to 3 $\mu m$ are propagated along the MMI waveguides with width in a range of 15 $\mu m$ to 60 $\mu m$. As shown in this figure, both the calculated POI and purity are enhanced by increasing in the waveguide's width and WR of the input mode. Figure 8 also demonstrates that for an specific waveguide width, an input mode with a larger WR leads to attain higher purity and POI. This is true for all orders of the input OAM modes. However, for higher order modes, the POI and purity have lower values. Thus, the utilization of this structure in higher order modes applications needs the input modes with higher values of WR to achieve reasonable amounts of the POI and purity.

It is worth mentioning that for the OAM modes with even values of $l$, the location of split fields at field splitting length of an MMI waveguide has different pattern with respect to the field patterns shown in figure 4 for the odd order OAM modes. Figure 9 shows the normalized power distributions of the split fields at length $3L_c/4$ of an MMI waveguide with $W = 40\ \mu m$

**Table 2.** The Calculated POI and purity for the mentioned waveguide in figure 7 with $W = 40 \ \mu m$ and the propagated OAM modes with $WR = 3 \ \mu m$.

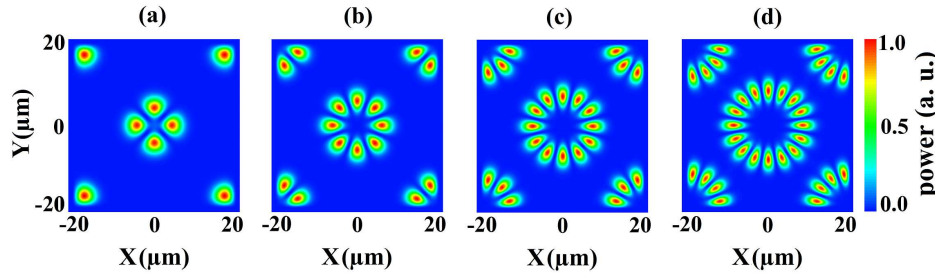| Topological Charge | POI (%) | purity (%) |
|:---:|:---:|:---:|
| $\pm 2$ | 98.66 | 92.43 |
| $\pm 4$ | 96.71 | 84.69 |
| $\pm 6$ | 93.93 | 79.27 |



**Figure 9.** Normalized power distributions of the split fields at the field-splitting length of an MMI waveguide with $W = 40$ $\mu m$ for the input OAM modes of $l = \pm 2$ (a), $l = \pm 4$ (b), $l = \pm 6$ (c), and $l = \pm 8$ (d).

for input OAM modes of $l = \pm 2$ (a), $l = \pm 4$ (b), $l = \pm 6$ (b), and $l = \pm 8$ (d). As shown in this figure, even OAM modes have been decomposed into fields located at four corners as well as the center of the MMI waveguides.

## Conclusion

In this paper, the propagation of OAM modes in square cross-sectional MMI waveguides is studied. Based on OAM-MMI theory, OAM modes form the field-splitting and OAM-maintaining images at distances $3L_c/4$ and $3L_c/2$ of an MMI waveguide, respectively. Utilizing MMI waveguides at these lengths for OAM integrated applications, the properties of generated images are investigated by considering the effects of three parameters including the width of the waveguide, the waist radius of the OAM mode and its topological charge. Accordingly, it is shown that the topological charge of odd order OAM modes remains unchanged at OAM-maintaining length, whereas the charge of even order modes is reversed. In other words, an MMI waveguide with the length $3L_c/2$ acts as charge converter for OAM modes with even values of $l$. In order to numerically confirm this fact, the simulations are performed using BPM method for silicon waveguides surrounded by silica which are compatible with silicon on insulator (SOI) technology. The waveguide is assumed to have width of 15 $\mu m$ to 60 $\mu m$, at working wavelength of 1550 $nm$. For OAM modes with odd values of $l$, the calculated POI along the waveguides between the input mode with WR in the range of 1.5 $\mu m$ to 3.5 $\mu m$ and the output produced mode demonstrate that the input modes with lower values of WR lead to make the completely split field profiles at field-splitting length which is desired for applications that use the benefits of wholly split fields. However, the propagated modes with lower values of WR need longer waveguides to give higher values of POI. For even order of OAM modes, the quality of the generated modes is evaluated by calculation of the purity as well as the POI for input OAM modes with WR in a range of 2 $\mu m$ to 3 $\mu m$. The results demonstrate that both the calculated purity and POI are enhanced by increasing in the waveguide's width and WR of the input mode. However, wider waveguides are longer. Therefore, the selection of a proper dimension for the waveguides to achieve a desired mode purity is a challenge. Consequently, this trade-off between the waveguide's dimension and the generated mode's purity should be considered carefully in the design procedures.

It is worth mentioning that due to the various applications of OAM modes in quantum and classical communications, the presence of optical integrated devices to manipulate these modes is necessary. According to the discussed properties of OAM modes in the investigated structure, as well as its passive and integrated nature, it has interesting potentials to be effectively used in OAM-based communication systems to facilitate the way into higher security and capacity systems.

## Data availability

All data generated or analysed during this study are included in this published article.

## References

1. Allen, L., Beijersbergen, M. W., Spreeuw, R. & Woerdman, J. Orbital angular momentum of light and the transformation of laguerre-gaussian laser modes. *Phys. review A* **45**, 8185 (1992).

2. Yu, S. Potentials and challenges of using orbital angular momentum communications in optical interconnects. *Opt. express* **23**, 3075–3087 (2015).

3. Wang, J. *et al.* Terabit free-space data transmission employing orbital angular momentum multiplexing. *Nat. photonics* **6**, 488–496 (2012).

4. Willner, M. J. *et al.* Reconfigurable orbital-angular-momentum manipulation and switching of polarization-multiplexed 100-gbit/s qpsk data channels. In *2013 IEEE Photonics Conference*, 1–2 (IEEE, 2013).

5. Liu, J., Li, S., Zhu, L. & Wang, J. Experimental demonstration of reconfigurable n× n joint orbital angular momentum (oam) and space switching fabric using a single spatial light modulator (slm). In *Asia Communications and Photonics Conference*, ASu2A–101 (Optical Society of America, 2015).

6. Longman, A. & Fedosejevs, R. Mode conversion efficiency to laguerre-gaussian oam modes using spiral phase optics. *Opt. express* **25**, 17382–17392 (2017).

7. Yan, L. *et al.* Q-plate enabled spectrally diverse orbital-angular-momentum conversion for stimulated emission depletion microscopy. *Optica* **2**, 900–903 (2015).

8. Gregg, P. *et al.* Q-plates for switchable excitation of fiber oam modes. In *2015 Conference on Lasers and Electro-Optics (CLEO)*, 1–2 (IEEE, 2015).

9. Zhao, Y. *et al.* Mode converter based on the long-period fiber gratings written in the two-mode fiber. *Opt. express* **24**, 6186–6195 (2016).

10. Carpenter, J., Thomsen, B. C. & Wilkinson, T. D. Optical vortex based mode division multiplexing over graded-index multimode fibre. In *Optical Fiber Communication Conference*, OTh4G–3 (Optical Society of America, 2013).

11. Thalhammer, G., Bowman, R. W., Love, G. D., Padgett, M. J. & Ritsch-Marte, M. Speeding up liquid crystal slms using overdrive with phase change reduction. *Opt. express* **21**, 1779–1797 (2013).

12. Luo, X.-W., Zhang, C., Guo, G.-C. & Zhou, Z.-W. Topological photonic orbital-angular-momentum switch. *Phys. Rev. A* **97**, 043841 (2018).

13. Cai, X. *et al.* Integrated compact optical vortex beam emitters. *Science* **338**, 363–366 (2012).

14. Strain, M. J. *et al.* Fast electrical switching of orbital angular momentum modes using ultra-compact integrated vortex emitters. *Nat. communications* **5**, 1–7 (2014).

15. Xiao, Q. *et al.* Generation of photonic orbital angular momentum superposition states using vortex beam emitters with superimposed gratings. *Opt. express* **24**, 3168–3176 (2016).

16. Gambini, F., Velha, P., Klamkin, J. & Faralli, S. Design of an integrated bragg-assisted tunable silicon microring for orbital angular momentum generation. In *Integrated Photonics Research, Silicon and Nanophotonics*, ITu3B–4 (Optical Society of America, 2016).

17. Fontaine, N. K., Doerr, C. R. & Buhl, L. L. Efficient multiplexing and demultiplexing of free-space orbital angular momentum using photonic integrated circuits. In *OFC/NFOEC*, 1–3 (IEEE, 2012).

18. Doerr, C. R. & Buhl, L. L. Circular grating coupler for creating focused azimuthally and radially polarized beams. *Opt. letters* **36**, 1209–1211 (2011).

19. Qin, C. *et al.* Demonstration of orbital angular momentum state conversion using two hybrid 3d photonic integrated circuits. In *Optical Fiber Communication Conference*, Th4A–1 (Optical Society of America, 2014).

20. Zhang, N. *et al.* Large-scale integrated reconfigurable orbital angular momentum mode multiplexer. *arXiv preprint arXiv:2008.00680* (2020).

21. Zhang, D., Feng, X., Cui, K., Liu, F. & Huang, Y. Generating in-plane optical orbital angular momentum beams with silicon waveguides. *IEEE Photonics J.* **5**, 2201206–2201206 (2013).

22. Zheng, S. & Wang, J. On-chip orbital angular momentum modes generator and (de) multiplexer based on trench silicon waveguides. *Opt. express* **25**, 18492–18501 (2017).

23. Liang, Y., Wu, H. W., Huang, B. J. & Huang, X. G. Light beams with selective angular momentum generated by hybrid plasmonic waveguides. *Nanoscale* **6**, 12360–12365 (2014).

24. Liang, Y., Zhang, F., Gu, J., Huang, X. G. & Liu, S. Integratable quarter-wave plates enable one-way angular momentum conversion. *Sci. reports* **6**, 1–8 (2016).

25. Ni, F. C., Xie, Z. T., Hu, X.-d., Jia, C.-y. & Huang, X. G. Selective angular momentum generator based on a graphene hybrid plasmonic waveguide. *J. Light. Technol.* **37**, 5486–5492 (2019).

26. Zhang, D. Angular momentum of optical modes in a silicon channel waveguide. *Phys. Rev. Res.* **2**, 033454 (2020).

27. Fatkhiev, D. M., Lyubopytov, V. S., Kutluyarov, R. V., Grakhova, E. P. & Sultanov, A. K. A grating coupler design for optical vortex mode generation in rectangular waveguides. *IEEE Photonics J.* **13**, 1–8 (2021).

28. Soldano, L. B. & Pennings, E. C. Optical multi-mode interference devices based on self-imaging: principles and applications. *J. lightwave technology* **13**, 615–627 (1995).

29. Chack, D., Hassan, S. & Kumar, A. Design and analysis of polarization beam splitter based on cascaded mmi on soi. In *Integrated Optics: Devices, Materials, and Technologies XXIV*, vol. 11283, 1128320 (International Society for Optics and Photonics, 2020).

30. Jiao, Y., Dai, D., Shi, Y. & He, S. Shortened polarization beam splitters with two cascaded multimode interference sections. *IEEE Photonics Technol. Lett.* **21**, 1538–1540 (2009).

31. Yao, Y., Wang, W. & Zhang, B. Designing mmi structured beam-splitter in linbo 3 crystal based on a combination of ion implantation and femtosecond laser ablation. *Opt. express* **26**, 19648–19656 (2018).

32. Wageeh, A., El-Sabban, S. & Khalil, D. Design of a 2d fiber mode converter using a planar 2d multi-mode interference structure. *Optik* **210**, 164500 (2020).

33. Nuck, M. *et al.* 3d photonic integrated 4x4 multi-mode interference coupler. In *Integrated Optics: Devices, Materials, and Technologies XXIII*, vol. 10921, 109211C (International Society for Optics and Photonics, 2019).

34. Zhou, Y. *et al.* Silicon-based mode converter and demultiplexer for wavelength division multiplexing transmission by using multimode interference couplers. *Opt. Photonics J.* **10**, 117 (2020).

35. Linh, H. D. T., Truong, D. C., Quang, D. D., Phuc, V. D. & Hung, N. T. Mode switch for on-chip optical interconnects using multimode interference couplers. In *2019 6th NAFOSTED Conference on Information and Computer Science (NICS)*, 98–102 (IEEE, 2019).

36. Jiang, X., Sun, Y., Yang, J. & Wang, M. General imaging properties of two-dimensional multimode interference couplers. *Opt. Eng.* **45**, 044602 (2006).

37. Ma, Z. *et al.* Self-imaging of orbital angular momentum (oam) modes in rectangular multimode interference waveguides. *Opt. express* **23**, 5014–5026 (2015).

38. Jiang, X., Mao, H. & Wang, M. Imaging properties and phase relations in mmi devices with two-dimensional confinement. In *Optical Fiber and Planar Waveguide Technology II*, vol. 4904, 51–56 (International Society for Optics and Photonics, 2002).

39. Khalil, D. & Yehia, A. Two-dimensional multimode interference in integrated optical structures. *J. Opt. A: Pure Appl. Opt.* **6**, 137 (2003).

40. Dashti, P. Z., Alhassen, F. & Lee, H. P. Observation of orbital angular momentum transfer between acoustic and optical vortices in optical fiber. *Phys. review letters* **96**, 043604 (2006).

41. Mousavi, S. F. & Nouroozi, R. On-chip enhanced electro-optic kerr effect for manipulation of optical orbital angular momentum modes. *J. Opt.* **22**, 075801 (2020).

## Author contributions statement

A.S. and R.N. conceived the idea. A.S. carried out the theoretical analysis, simulation and writing the manuscript. All authors reviewed the manuscript and discussed the results.

## Additional information

**Competing interests:** The authors declare that they have no competing interests.